Article

Carbon Embedding of Pt Cluster Superlattices Templated by Hexagonal Boron Nitride on Ir(111)

Tobias Hartl,* Moritz Will, Pantelis Bampoulis, Daniel Herrmann, Philipp Valerius, Charlotte Herbig, Virginia Boix de la Cruz, Paolo Lacovig, Vedran Vonk, Simon Chung, Andreas Stierle, Silvano Lizzit, Jan Knudsen, and Thomas Michely

Read Online

ACCESS | Metrics & More | Article Recommendations | SI Supporting Information

ABSTRACT: With the goal to delevop the fabrication of a new type of Pt-nanoparticle carbon−support electrocatalyst, we investigate the carbon embedding of Pt cluster superlattices grown on the moiré of a monolayer of hexagonal boron nitride (h-BN) on Ir(111). Our combined scanning tunneling microscopy (STM) and X-ray photoelectron spectroscopy (XPS) study establishes conformal C embedding of the Pt clusters on h-BN/Ir(111) without deterioration of superlattice order, preferential and strong binding of the embedding carbon to the Pt clusters, and upon annealing the formation of a homogeneous amorphous carbon (a-C) matrix. There are indications that while the a-C matrix and the Pt clusters bind strongly to each other, upon annealing both weaken their binding to h-BN.
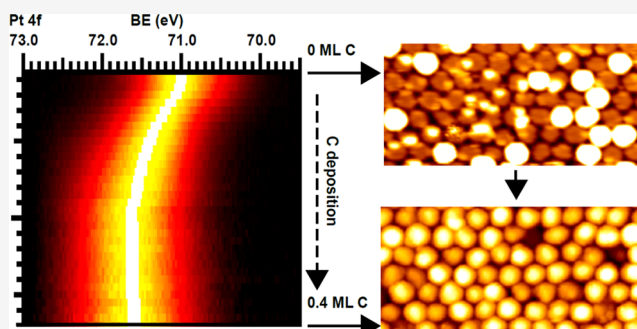
INTRODUCTION

Novel 2D materials and material systems offer new research opportunities and applications. Examples range from the magic angle bilayer graphene (Gr) that displays superconductivity[1] to carbon nanomembranes that offer new ways for efficient filtering of gases and liquids.[2,3]

Recently, a first example of a cluster superlattice membrane (CSLM) was fabricated: a new 2D material consisting of a superlattice of similar sized Ir clusters sandwiched between Gr and an amorphous carbon matrix.[4] The fabrication of this material is based on (i) the templated growth of a superlattice of clusters atop the moiré of a 2D material, e.g., Gr, with a metal substrate, (ii) the embedding of the cluster superlattice into a matrix, e.g., amorphous carbon (a-C), and (iii) the lift-off of the hybrid material from the substrate. CSLMs have potential for new research opportunities in nanocatalysis. For the case of a Pt superlattice, once the 2D layer is stripped off from the membrane, an a-C membrane with very densely spaced Pt catalyst particles of similar size would result. Because of the unique synthesis method, the Pt particles are size-tunable to the atomic limit. As we will show, the Pt particles can be expected to be firmly bound to the a-C matrix and assumed to resist aggregation even under harsh conditions. These properties would make such a membrane an attractive electrocatalyst for fuel cell research.[5,6]

In the present work we investigate a decisive step in the formation of a Pt cluster superlattice membrane, namely, the embedding into an a-C matrix. The complementary chemical information from XPS and structural information from STM yields a comprehensive picture of the embedding process.

Pt cluster superlattices were templated previously on Gr/Ir(111),[7,8] Gr/Ru(0001),[9] alumina films on Ni₃Al(111),[10] monolayer hexagonal boron nitride on Rh(111),[11,12] and h-BN on Ir(111).[13] Here we investigate the carbon embedding for Pt/h-BN/Ir(111) because this system has excellent superlattice order and high sintering resistance (no effect up to 650 K)[13] which make it an attractive candidate for CSLM formation. Because all components of the system (substrate, 2D-layer, clusters, and embedding matrix) are composed of different elements, the chemical processes during carbon embedding can be tracked without ambiguity through XPS. The present study extends our previous combined XPS/STM investigation of binding and thermal stability for Pt/h-BN/Ir(111)[13] and compares to our carbon embedding investigation for Ir/Gr/Ir(111).[14] The latter had the disadvantage of having the embedding matrix and the 2D-layer being composed of the same chemical element, C, making it difficult to disentangle the processes with XPS.
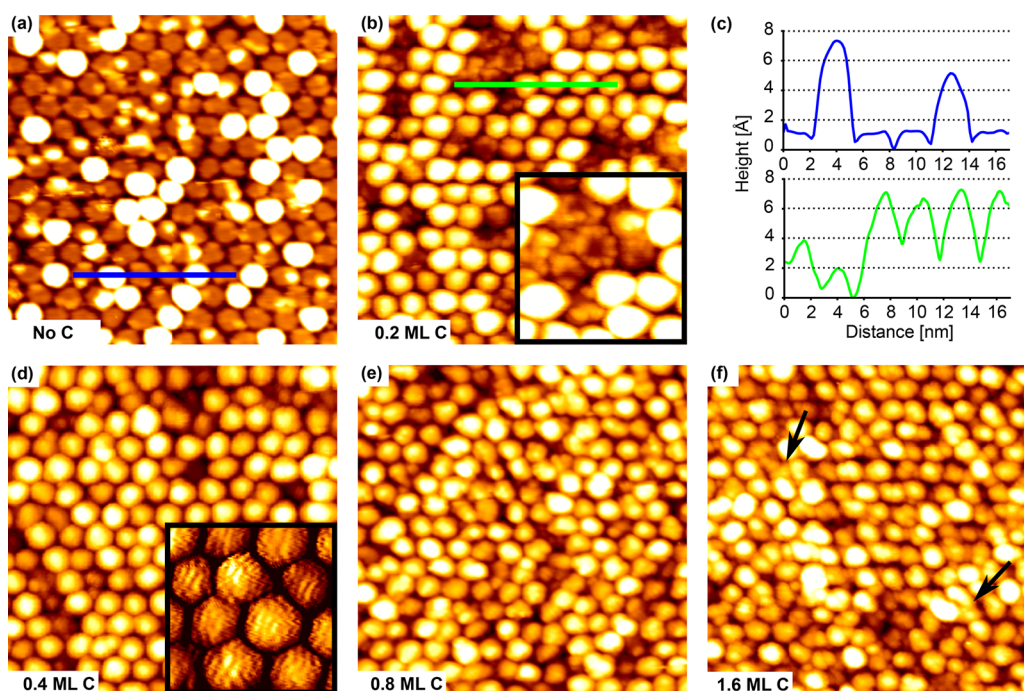
Figure 1. STM topographs of Pt cluster superlattices on h-BN/Ir(111) formed by deposition of 0.55 ML Pt at 300 K (a) without and (b, d−f) with additional C deposited. Carbon amounts are (b) 0.2, (d) 0.4, (e) 0.8, and (f) 1.6 ML. (c) shows the height along the blue line in (a) and the green line in (b). The inset in (d) is a composite of the topograph and its derivative to increase the contrast of the molecular orbital resolution (see text). The image size is 34 nm × 34 nm in all cases.

Here we thoroughly investigate the structural evolution and the changes in binding between the different membrane components upon increasing amounts of carbon deposited and upon additional thermal annealing. Our investigation establishes not only conformal C-embedding of the Pt clusters on h-BN/Ir(111) without deterioration of superlattice order but also an excellent thermal stability of the embedded Pt superlattice up to 850 K.

Before we present our results, we briefly summarize the knowledge on the h-BN/Ir(111) and Pt cluster superlattices templated thereon to prepare for the results presented below. H-BN/Ir(111) forms a moiré superstructure with (11.7 × 11.7) h-BN unit cells matching (10.7 × 10.7) Ir surface unit cells, which results in a 29.1 Å repeat distance. The layer displays one chemisorbed and reactive valley in each moiré unit cell within an otherwise flat, physisorbed mesa.[15] In the valleys, defined by the locations in the moiré where N atoms sit atop Ir substrate atoms, the sp^2-hybridized h-BN displays partial sp^3 character whereby bonds with the Ir substrate and a reactive spot toward the vacuum are formed.[15] Note that an sp^3-hybridized layer displays σ-bonds normal to the layer into both half-spaces. Upon deposition of Pt, clusters are formed in the reactive valleys, whereby the sp^3 binding motif is modified and strengthened. Pt clusters are stable against sintering up to 650 K, while for higher temperatures the superlattice decays through intercalation and cluster coalescence.[13]

■ METHODS

STM was conducted in the ultrahigh-vacuum system Athene in Cologne, and XPS data were recorded at the SuperESCA beamline of Elettra, the synchrotron radiation facility in Trieste, Italy. The base pressure of both systems is in the 10^{-11} mbar range. Ir(111) was cleaned by O_2 glowing at $T = 1100$ K in a pressure of $p_{O_2} = 1 \times 10^{-6}$ mbar for 600 s, followed by

sequences of 2 keV noble gas sputtering and flash annealing to 1500 K.

A gas dosing tube with a pressure enhancement factor of 80 compared to the readout of the ion gauge was used for growth of h-BN in Cologne. At 1250 K the sample was exposed to an ion gauge pressure of $p = 5 \times 10^{-9}$ mbar of borazine ($B_3H_6N_3$) for 30 s, resulting in well-oriented h-BN monolayer islands. Areas without h-BN coverage were later used to calibrate the deposited amount of Pt. At Elettra the borazine pressure was increased to 1×10^{-6} mbar, as no gas dosing tube was installed and the time was increased to 300 s. The absence of room temperature CO adsorption in the XP spectra was used to confirm a 1 ML coverage of h-BN. The h-BN was shown to consist of well-ordered domains via low-energy electron diffraction, both in Cologne and in Trieste.

Pt or C was deposited on the sample from a multiple e-beam evaporator at a typical rate on the order of 5×10^{-3} ML/s, with the Pt ML corresponding to a full layer of pseudomorphic Pt on Ir(111) and the C ML to a fully closed Gr layer. The pressure remained below 2×10^{-10} and 2×10^{-9} mbar during Pt and C deposition, respectively. To enable fast XPS measurements of the sample during deposition, the evaporator was mounted adjacent to the analyzer. The deposition rates were calibrated by determination of the coverage of either Gr or pseudomorphic Pt islands formed on Ir(111) via STM in Cologne with a relative error of about 5% and via the intensity of the C 1s core level in relation to the Ir 4d core level in Trieste with a relative error of 15%.

STM was conducted at room temperature with tunneling currents on the order of $I = 0.5$ nA and a sample bias in the range of $V = \pm 2$ V. STM images have been processed by using the WSxM software.[16]

All XP core level spectra were measured in normal emission with an energy resolution better than 50 meV. Ir 4f and Pt 4f

spectra were recorded at a photon energy of $h\nu = 140$ eV, C 1s spectra were measured at $h\nu = 390$ eV, B 1s at $h\nu = 320$ eV, and N 1s at $h\nu = 500$ eV. After calibration of the binding energy (BE) to the Fermi edge a polynomial background was subtracted from the data. Doniach−Ŝunjić functions convoluted with a Gaussian were used to fit the Ir, C, and N spectra. The Pt core level was fitted with asymmetric pseudo-Voigt functions.

XRD data shown in the Supporting Information were collected at beamline P23 of Petra III/DESY in Hamburg. The sample was prepared in Cologne, exposed to ambient conditions, and later reintroduced into a vacuum of $p = 10^{-8}$ mbar in Hamburg.

■ RESULTS AND DISCUSSION

Carbon Embedding Characterized by STM. For reference, Figure 1a displays a cluster superlattice on h-BN/Ir(111) after deposition of 0.55 ML Pt at 300 K, without any additional carbon deposition. Each moiré unit cell contains precisely one Pt cluster with a (111) plane parallel to the substrate. Although the clusters are of similar size in atom number with an average of $s_{av} = 63 \pm 8$ atoms per cluster, only clusters of monolayer and trilayer height or above are visible. The height distribution and lack of two layer clusters are a consequence of the collapse of metastable monolayer clusters on the h-BN/Ir(111) moiré as described by Will et al.[13]

Upon deposition of 0.2 ML carbon, many clusters reshape into a multilayer configuration. Remaining monolayer clusters (roughly 15%) show clear signs of carbon adsorption, with carbon decorating the rim of the monolayer clusters as visible in the inset of Figure 1b. Figure 1c shows the line profiles before the deposition of C (blue) and after the deposition of 0.2 ML C (green). Note that the baseline of height in the profiles is somewhat uncertain, as the tip does not reach down to the Gr with certainty. At 0.4 ML carbon deposited (Figure 1d), the cluster superlattice has become more uniform in cluster shape. Molecular orbital resolution, stemming from the adsorbed carbon, is now visible. Still all clusters are distinct and confined to their own moiré unit cell. At higher coverages of 0.8 or 1.6 ML, represented by Figures 1e and 1f, the carbon starts to fill in the space between the clusters and to form a network (see arrows in Figure 1f). Based on the STM topographs, there is no indication that the order of the cluster superlattice is disturbed by C embedding. This is supported by the SXRD data presented in Figure S1 of the Supporting Information, where an Ir cluster superlattice embedding on h-BN/Ir(111) was investigated.[17] In conclusion, the carbon embedding of the Pt cluster lattice on h-BN/Ir(111) proceeds similar as for an Ir cluster lattice on Gr/Ir(111) investigated in ref 14.

Carbon Embedding Analyzed by XPS. XPS measurements, following C deposition, were performed for a Pt cluster superlattice formed by deposition of 0.1 ML Pt on h-BN on Ir(111). The Ir $4f_{7/2}$ core level of the substrate was measured and fitted with three components: Ir$_B$ attributed to the Ir bulk atoms at the binding energy 60.86 eV (blue in Figure 2a), Ir$_S$ attributed to Ir surface atoms without bonds to h-BN or adsorbates at 60.34 eV (brown in Figure 2a), and Ir$_{int}$ attributed to Ir surface atoms chemically binding to the h-BN at 60.63 eV (ochre in Figure 2a), following the approach of Orlando et al. in ref 18. From the comparison of the two data points in Figure 2b for the relative intensity of Ir$_{int}$ at zero carbon coverage, it is obvious that the interface component is
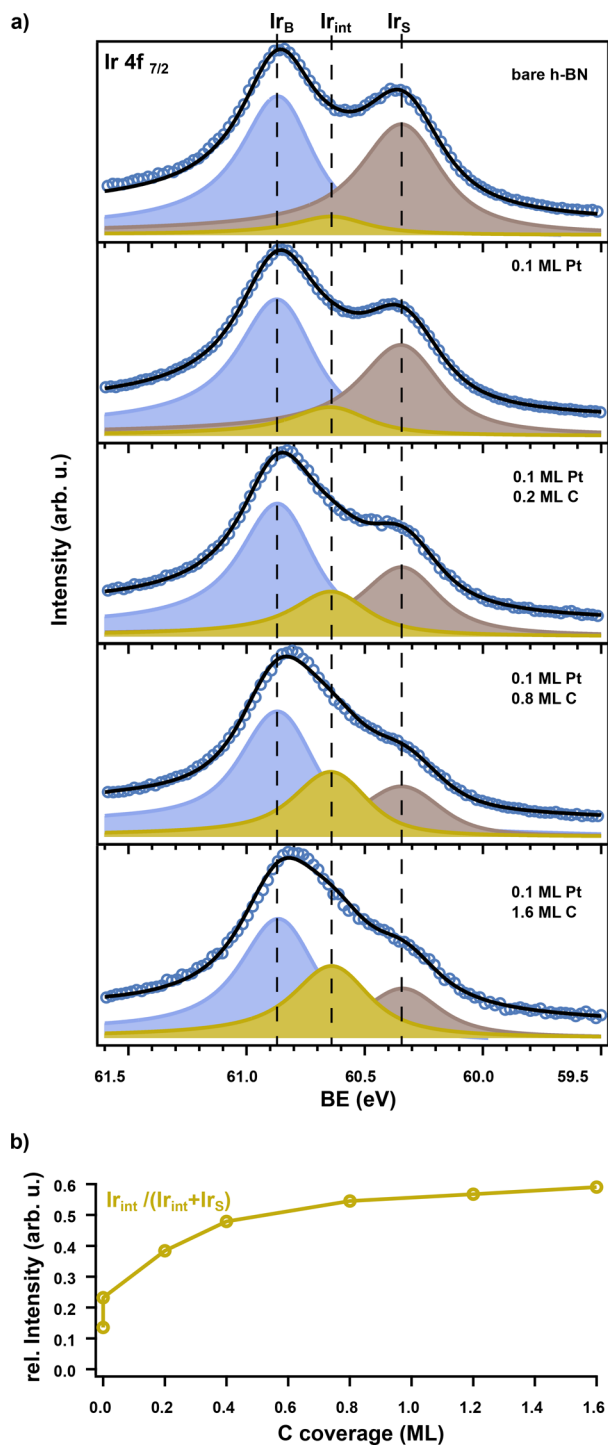
Figure 2. (a) XP spectra of the Ir $4f_{7/2}$ core level of the Ir(111) substrate with a monolayer of h-BN and after subsequent deposition of 0.1 ML Pt and increasing amounts of carbon measured at a photon energy of $h\nu = 140$ eV at room temperature. The measured data are indicated by blue circles, and the fit is a black line. From top to bottom: pristine h-BN prior to deposition, after deposition of 0.1 ML Pt resulting in bare clusters and after embedding in 0.2, 0.8, and 1.6 ML carbon. (b) Intensity of the interface component (Ir$_{int}$) normalized to the sum of the interface and surface component (Ir$_{int}$ + Ir$_S$) as a function of carbon coverage. The lower and upper data points at zero coverage represent the system before and after deposition of 0.1 ML Pt, respectively.

already increased by deposition of 0.1 ML Pt when compared to pristine h-BN on Ir(111). This is due to the formation of Pt clusters, which enlarge the moiré valleys and thus the sp^3-hybridized h-BN areas binding to Ir surface atoms.[13,19] After the deposition of 0.2 ML C, the Ir_{int} component has grown significantly at the expense of the Ir_S component. In good agreement with the observed behavior in the STM topographs, the increase in intensity of the I_{int} peak normalized to the intensity from all Ir surface atoms slows down significantly above 0.8 ML C (Figure 2b), indicating that from this point on the changes taking place are mostly carbon−carbon based interactions. The increase of Ir_{int} implies an increase of sp^3 hybridization of h-BN, which in turn has to be triggered by chemical bond formation between C and the h-BN sheet. We will see below that these bonds are formed predominantly at the cluster rim.

During carbon embedding the Pt $4f_{7/2}$ core level was monitored via fast-XPS with a time resolution of 1 min per spectrum. As obvious from Figure 3, a significant shift of the
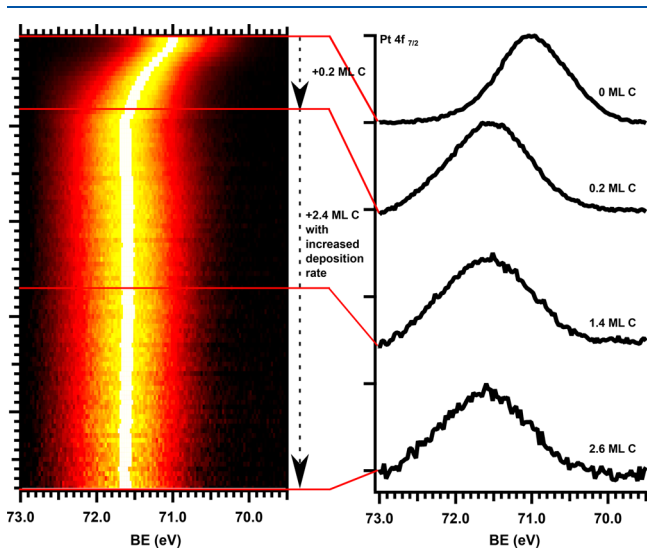

Figure 3. Time-resolved XP spectra of the Pt $4f_{7/2}$ core level during the embedding process of a 0.1 ML Pt cluster superlattice on h-BN/Ir(111). Selected spectra are displayed on the right as line profiles for C coverages of 0, 0.2, 1.4, and 2.6 ML, from top to bottom.

BE from 71.0 to 71.6 eV takes place during the initial stages of the carbon deposition, accompanied by a broadening of the peak. Beyond a C coverage of 0.2 ML the peak position and width remain constant. We interpret these changes as follows: Initially, the deposited C preferentially covers the Pt clusters, similar to the C embedding of iridium clusters.[14] These Pt−C bonds cause a rapid change of the Pt 4f level up to 0.2 ML C deposited. Then, the clusters are entirely covered, and no more changes of the Pt 4f core level take place.

To obtain insight into the formation of the embedding carbon matrix, the C 1s core level was measured after stepwise deposition of carbon on the cluster superlattice as shown in Figure 4. Because of the multitude of possible binding configurations, the C 1s peak is notoriously difficult to fit for C in an inhomogeneous environment. Here we simplify the situation through a four component fit as shown for the spectrum in Figure 4a, which was recorded after 0.2 ML C deposition. The first component C_{sp^1} at 283.55 eV is attributed to carbon in an sp^1 configuration, that is, linear carbon

multimers or C bound with single bonds to Pt.[20,21] Note that the majority of carbon species in the vapor arriving at the surface are linear carbon trimers.[22] The components C_{sp^2} at 284.1 eV and C_{sp^3} at 285 eV result from sp^2 (graphitic) or sp^3 (diamond-like) hybridized carbon atoms.[7,23,24] The origin of a broad fourth component C_X, fitted at a BE of 286.9 eV, and of a fifth component C_B indicated in Figure 4a, but not fitted, will be discussed below. The increase in carbon coverage allows the carbon to form bonds to other carbon atoms shifting the intensity from the original C_{sp^1} into the C_{sp^2} and C_{sp^3} components. Figure 4b displays the C 1s spectrum with the same components fitted to it as in (a) after the deposition of 1.6 ML C. The C_{sp^1} component is significantly decreased, while the increase of the C_{sp^2} and C_{sp^3} components signifies that the embedding matrix is an amorphous carbon film with a mixture of sp^2 and sp^3 bonding. The plot of the relative intensities of the fitted components in Figure 4d confirms that the membrane consists of a network of sp^2- and sp^3-bonded carbon. The relative and absolute intensity of C_{sp^1} drops because the ratio of carbon in direct contact with the Pt clusters and the h-BN surface shrinks and sp^1-bonded multimers are integrated into the network, as more and more carbon is deposited.

The broad component C_X, not discussed yet, covers two carbon configurations. First, we have evidence for a slight CO adsorption on clusters from the O 1s core level (data not shown). The corresponding C 1s signature for CO is in the range of 286.9 eV, matching roughly the BE of C_X.[25] Moreover, C that forms C−N bonds contributes to C_X. The BE of C−N bonds in the C 1s core level was found to be 287.1 eV, matching the position of C_X quite well.[26] Further evidence for the formation of C−N bonds stems from the analysis of the N 1s core level, discussed below. As expected, the relative intensity of C_X drops with increasing amount of C deposited (compare Figures 4b and 4d).

Figure 4a also indicates a component C_B, which has not been fitted, with an estimated BE of 281.5 eV. It decreases with an increase in coverage and appears to vanish at a coverage of 0.8 ML f C (compare Figure 4c). A peak at the same energy and with similar intensity is also present in the C 1s core level spectrum after 0.3 ML carbon deposition on bare h-BN, in the absence of metal clusters (compare Figure S2). A peak with similar binding energy has been observed in C 1s spectra of compounds with a low carbon to boron ratio.[27,28] Even though the origin of this peak cannot rigorously be deduced, we propose that the peak stems from single C atoms initially forming bonds to the B and disappears when the C is incorporated into the matrix, forming bonds to other C atoms and gaining more of an sp^2/sp^3 character.

The last chemical signatures monitored during embedding are the N 1s and B 1s core levels of the h-BN, shown in Figures 5a and 5b. As h-BN remains intact as a 2D material upon adsorption, changes in both signals are subtle. The broadening of the N 1s and B 1s peaks with C deposition indicates an increased chemical variety of the boron and nitrogen bonds, caused by the interaction of the h-BN layer with the carbon. As obvious from the quantitative analysis of the evolution of the full width at half-maximum (FWHM) with C coverage, the broadening is significantly slowing down as the coverage reaches 0.8 ML (Figure 5c). For 0.8 ML C the h-BN is almost
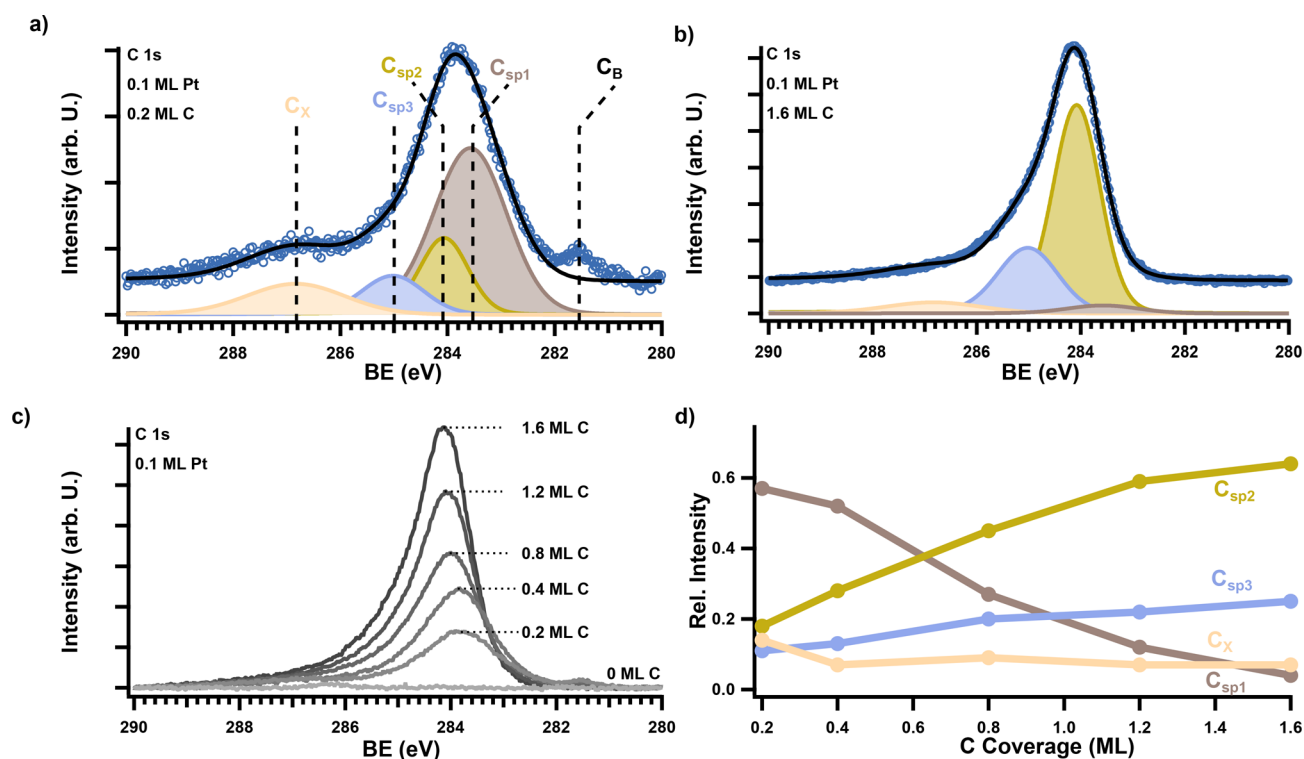
Figure 4. (a, b) XP spectra of the C 1s core level of the embedding carbon covering a 0.1 ML Pt cluster superlattice on h-BN/Ir(111): (a) after embedding in 0.2 ML C and (b) 1.6 ML C. As fit components C_{sp^1} (brown), C_{sp^2} (ochre), and C_{sp^3} (blue) of sp^1-, sp^2-, and sp^3-bonded carbon at BEs of 283.55, 284.1, and 285 eV were used, respectively. An additional component C_X (beige) centered at a BE of 286.9 eV is used to fit the shoulder at the high-energy side (see text). Additionally an unfitted component C_B at a BE of 281.5 eV is indicated (see text). (c) XP C 1s core level spectra after increasing amounts of C deposited on Pt/h-BN/Ir(111). (d) Change of the relative intensities of the fit components in (a, b) as a function of carbon coverage. Lines to guide the eye.

completely covered by C, and newly arriving C binds to already deposited C rather than to h-BN.

The N 1s core level spectrum is fitted with three components. The first two are the N_{mesa} component at 397.62 eV and the N_{valley} component at 398.50 eV, as introduced by Orlando et al.[18] for bare h-BN on Ir(111). The third component N_C, located at the binding energy of 399.4 eV, evolves with carbon deposition (see Figure 5e) and is attributed to carbon−nitrogen bonds, consistent with Yan et al.[26] N atoms contributing to this component form bonds with C atoms, which correspond to the C 1s C_X component introduced above. From the intensity of the N_C component it is obvious that only a small fraction of N atoms of the h-BN bind to C atoms (Figure 5e).

Altogether, the XPS data suggest three stages of C embedding for the Pt cluster superlattice. (i) Initially, the deposited C binds preferentially to the Pt clusters and the rehybridized h-BN area along their rim. The small Pt clusters are well saturated with carbon already after deposition of 0.2 ML (compare Figure 3a), and at the rim C−N and C−B bonds are formed (Figure 5c), which reflect through the sp^3 binding motif of h-BN also down to the Ir substrate (Figure 2a). (ii) Upon subsequent deposition more C−N and C−B bonds are formed, but as the geometry for rehybridization is less favorable in the mesa, the induced changes slow down (compare Figures 2a and 5c). (iii) Beyond 0.8 ML deposited essentially the entire h-BN layer including the clusters are covered by C. Therefore, further C deposition leaves the Ir 4f, the B 1s, and N 1s core levels unchanged (compare Figures 2b

and 5c). The closed C film grows in thickness, and changes are only present in the C 1s core level (compare Figure 4).

Annealing and Thermal Stability of an Embedded Cluster Superlattice on h-BN. Besides of fundamental interest, the thermal stability of embedded cluster superlattices is of decisive importance for their subsequent use. Specifically, lift-off of an embedded cluster superlattice from the metal substrate for application in nanocatalysis requires in the case of the Gr/Ir(111) intercalation at elevated temperatures and annealing up to 850 K.[4] A similar requirement is to be expected for the membrane lift-off from the h-BN/Ir(111) template.

Figure 6 displays STM topographs of an annealing sequence for a 0.55 ML Pt cluster superlattice, embedded with 1.6 ML carbon. The sample without annealing is shown in Figure 6a as a reference. The visible order decreases at 850 K as shown in Figure 6b. The clusters are mostly intact. No large-scale sintering has taken place, as in the case of bare cluster superlattices.[13] Further annealing to 1050 and 1250 K as shown in Figures 6c and 6d hardly changes the morphology, and even at the highest annealing temperature the carbon cover of the clusters stays intact. The stability of the embedding matrix is quite similar to the case of carbon embedding of Ir cluster superlattices on Gr/Ir(111).[14] However, STM imaging is limited to the embedding matrix, and no information about the encased Pt clusters can be inferred from these topographs.

To gain information about the thermal stability of embedded clusters themselves, fast-XPS measurements of the Pt 4f$_{7/2}$ core level spectrum of a 0.1 ML Pt cluster superlattice were taken
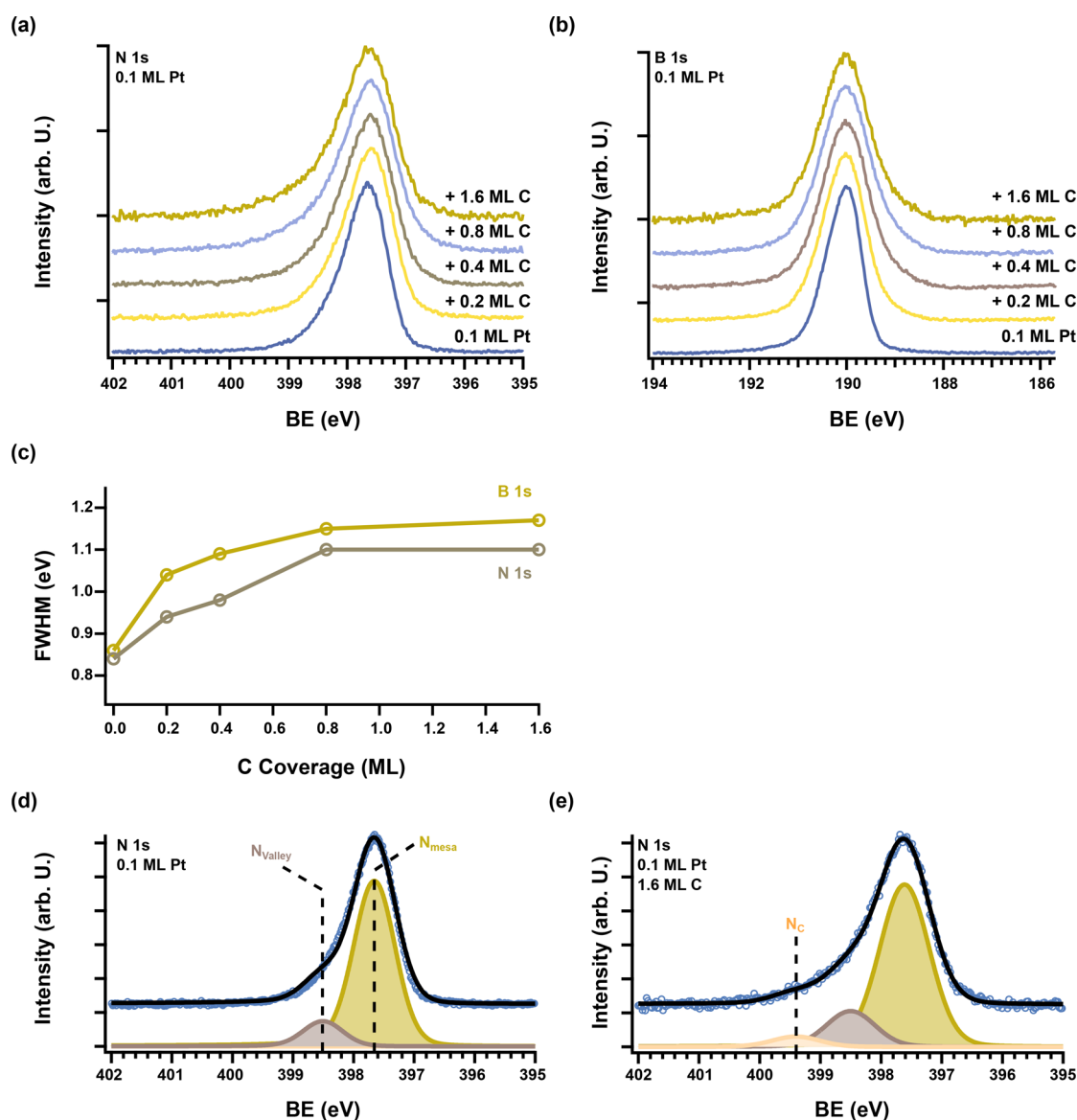
Figure 5. (a, b) Normalized spectra of the (a) N 1s and (b) B 1s peaks of h-BN on Ir(111) with a 0.1 ML Pt cluster superlattice and after stepwise deposition of carbon. (c) Full width at half-maximum of the B 1s and N 1s peaks as a function of carbon coverage. (d, e) Three-component fit of the N 1s peaks of (d) without and (e) with an additional 1.6 ML carbon deposited.

during annealing of the sample as shown in Figure 7a. Two effects of the annealing are visible: A gradual shift toward lower binding energies sets in above 600 K and is finalized at 1000 K. At high temperatures the peak also becomes narrower in the region around its maximum. After the sample has reached 1200 K the heating was switched off, and fast XPS measurements continued during cooling of the sample to 500 K (see bottom part of Figure 7a). During cooldown, thermal broadening diminishes and consequently the Pt $4f_{7/2}$ peak sharpens, without changing its position. The core level shift by about 350 meV toward lower binding energy and the sharpening of the peak indicate irreversible changes in the cluster superlattice.

For quantitative analysis high-resolution spectra after stepwise flash annealing and subsequent cooling to room temperature are more suitable, as thermal broadening is largely absent and equal for all spectra. Figure 7b displays four such spectra fitted with two components: The first component $Pt_{cluster}$ (ochre) is attributed to Pt atoms in the clusters on h-BN, initially centered at 71.8 eV, with freedom to move to

lower binding energies. It matches in FWHM and energetic position the core level spectrum of the unannealed and embedded Pt cluster superlattice, shown as the first spectrum in Figure 7b. The second component, Pt_{int}, is attributed to Pt atoms that escaped from their carbon cages and now are intercalated and in direct contact with Ir, as either monolayer island or surface alloy. Its width and energetic position at 71.0 eV are chosen to be identical with the width and energetic position of Pt deposited directly onto Ir(111) and annealed to 1250 K, as shown in the core level spectrum of Figure 7c. We note that the component Pt_{int} cannot be attributed to bulk-like Pt in large compact clusters on h-BN, as according to Figure 6d even after annealing to 1250 K no such clusters formed.

At 850 K the cluster component has slightly shifted in BE down to 71.55 eV, and a small percentage (<5%) of Pt has intercalated. The downshift in binding energy at 850 K is likely to be caused by a reconfiguration of carbon bonds in contact with cluster metal. During this process the bonds are changed, but not lost, as the bare Pt clusters exhibit a BE maximum at
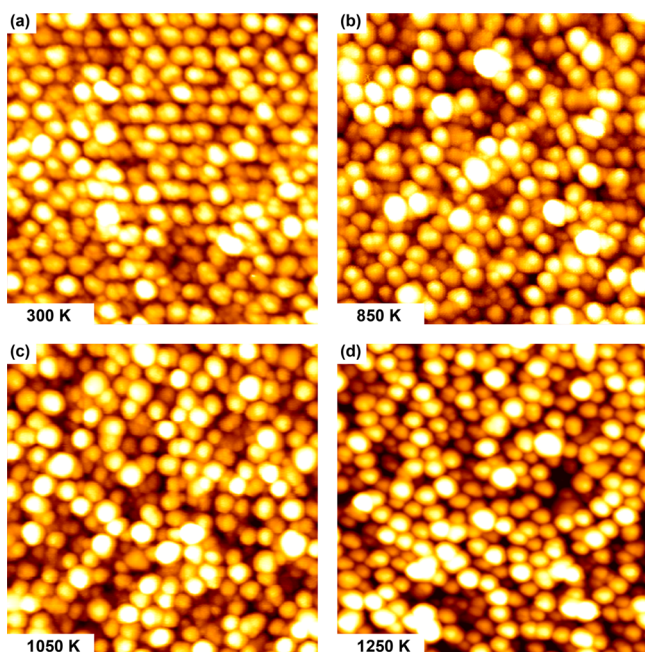
Figure 6. STM topographs of an embedded Pt cluster superlattice, formed by 300 K deposition of 0.55 ML Pt and 1.6 ML C on h-BN/Ir(111): (a) as grown and embedded at room temperature, (b) after annealing to 850 K, (c) after annealing to 1050 K, and (d) after annealing to 1250 K. All images are 34 nm × 34 nm.

71.0 eV. After annealing to 1050 K roughly 15% of the Pt has intercalated, increasing up to 50% at 1250 K as apparent from Figure 7d. The Pt_{int} signal is additionally attenuated by the h-BN layer, while the $Pt_{cluster}$ is not. In Figure 7d we corrected the intensity for this via $Pt_{int} = Pt_{int,0} \times \exp[d/\lambda]$, with $d = 3.3$ Å, the distance between h-BN and the Ir(111) surface,[15] and λ

= 9 Å, the inelastic mean free path, as described in ref 29. Further photoelectron diffraction effects were ignored in this analysis.

Evidently, intercalation is the key decay mechanism of a CSLM based on a monolayer of hexagonal boron nitride. The driving force for intercalation is the substantial energy gain, when the cluster Pt penetrates h-BN and becomes adsorbed to Ir(111). For a CSLM lifted off and flipped around such that the h-BN layer is facing the vacuum, the situation is evidently changed. The cluster metal does not find a better binding site after penetration of the h-BN layer, but just the vacuum. When additionally the amorphous carbon matrix is made thick, e.g., 10 ML instead of 1.6 ML, also penetration of cluster material through the matrix to the new substrate is suppressed. Thus, a higher thermal stability of the CSLMs in this situation can be expected.

The mechanism of Pt intercalation into the space between Ir(111) and h-BN remains elusive. Intercalation through preexisting point defects is one obvious possibility. Such point defects exist in substantial number for h-BN/Ir(111) (compare Figure 4b of ref 19). For the isostructural material Gr and for graphite, point defects were indeed proven to be of crucial relevance for the intercalation of many transition and rare earth metals.[30−34] A second possible mechanism of intercalation is etching of the encaged Pt metal through the h-BN layer, i.e., high-temperature creation of defects enabling permeation. In fact, metal adatoms were shown to lower the vacancy formation energy in Gr substantially.[35]

The evolution of the C 1s component during stepwise annealing, plotted in Figure 8, is indicative of a reorganization of the amorphous carbon membrane into a homogeneous amorphous carbon film with a high sp² content with increasing temperature. A fit of the data using the same components as for the core level spectra taken during embedding in Figure 4
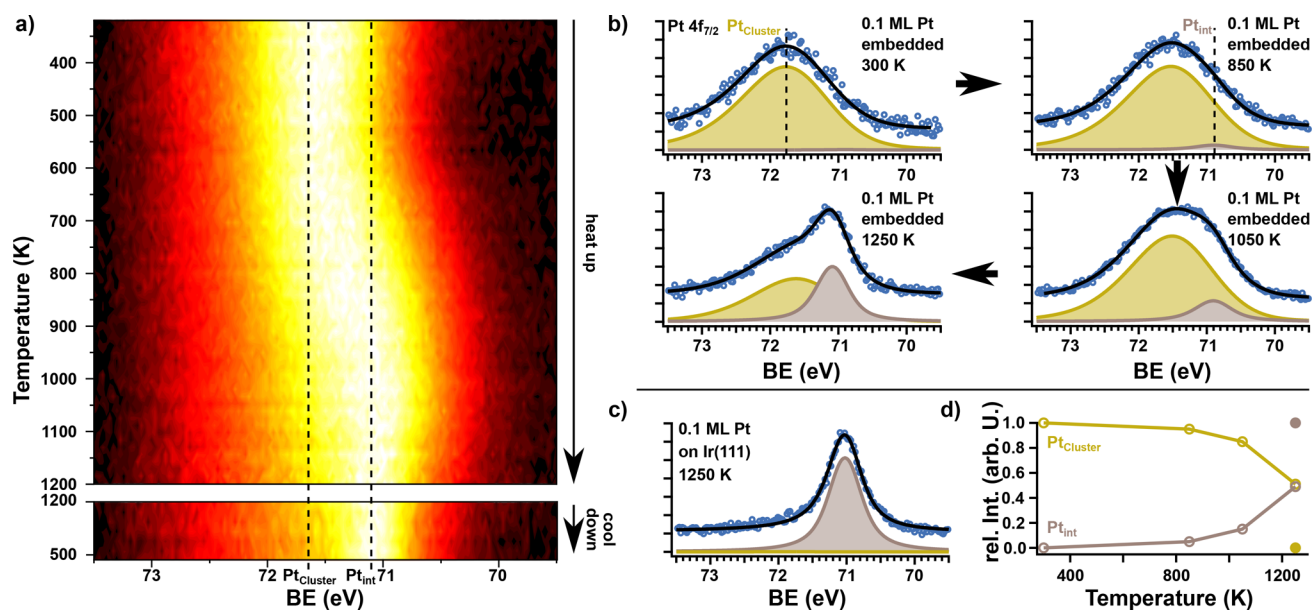

Figure 7. (a) Time-resolved normalized XP spectra of the Pt $4f_{7/2}$ core level during annealing of a 0.1 ML Pt cluster superlattice embedded in 1.6 ML C from 400 to 1200 K (top panel) and subsequently cooling to 500 K (bottom panel). (b) High-resolution spectra of the Pt $4f_{7/2}$ core level fitted with the components $Pt_{cluster}$ for Pt in clusters and Pt_{int} for intercalated Pt. (c) High-resolution spectrum of the Pt $4f_{7/2}$ peak of 0.1 ML Pt directly deposited on Ir(111), annealed to 1250 K, and cooled to RT. (d) Relative intensities of the two components as a function of annealing temperature. The filled circles at 1250 K correspond to the direct Pt on Ir(111) deposition and the open circles to the Pt clusters on h-BN. Lines are to guide the eye.
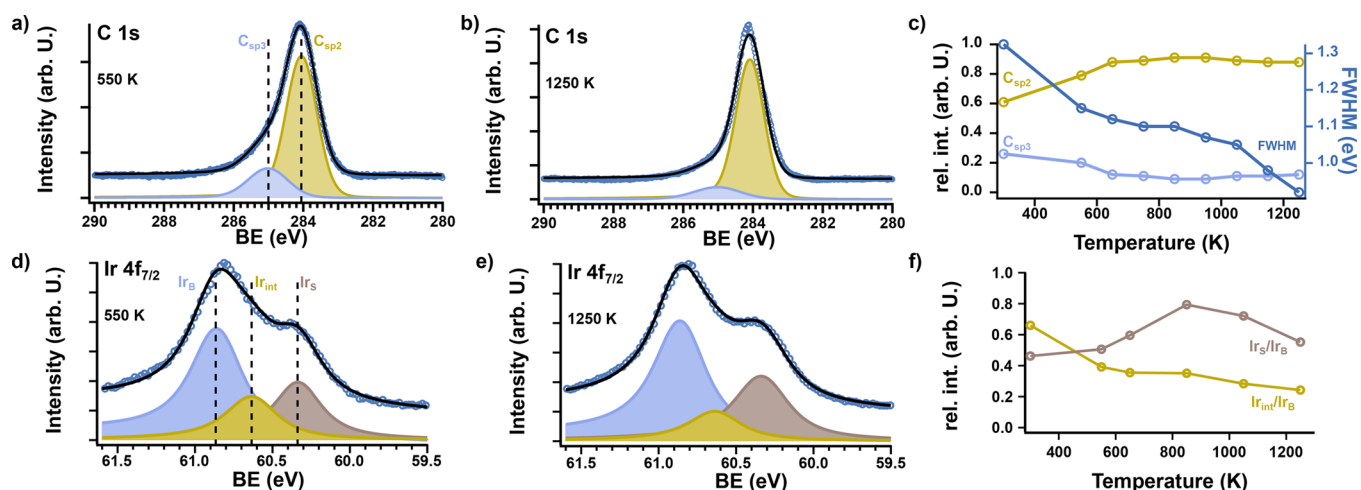
Figure 8. (a, b) XP spectra of the C 1s core level after annealing the 0.1 ML Pt cluster superlattice embedded in 1.6 ML C to (a) 550 K and (b) 1250 K, fitted with the components C_{sp^2} and C_{sp^3} (compare Figure 4). (c) Changes in the integrated relative intensities of the C_{sp^2} and C_{sp^3} components (left *y*-axis) as well as the total FWHM of the peak (right *y*-axis) as a function of annealing temperature. (d, e) Spectra of the corresponding Ir $4f_{7/2}$ core levels of the substrate. The fit uses the same components Ir_B, Ir_S, and Ir_{int} as for the core level spectra in Figure 2. (f) Relative intensities of Ir_S/Ir_B and Ir_{int}/Ir_B plotted as a function of annealing temperature. Lines are to guide the eye.

reveals already after annealing to 550 K (Figure 8a) that the spectrum can be described by only the two components C_{sp^2} and C_{sp^3}. The C_{sp^1} and C_X components have completely vanished. The disappearance of C_{sp^1} shows that the remaining sp^1-hybridized C has integrated into the C network forming sp^2 or sp^3 bonds, whereby the membrane is stabilized. The disappearance of the C_X component can be traced back to two changes. For CO, which might be trapped in the membrane, the increase in temperature leads to desorption. Moreover, the C−N bonds, which we proposed to contribute to C_X, are apparently broken due to the reorganization of carbon into more favorable bond configurations. The fit after annealing to 1250 K shown in Figure 8b shows that at this point the peak of the C 1s core level has significantly sharpened and consists mostly of sp^2-hybridized carbon. Figure 8c gives the relative integrated intensities of C_{sp^2} and C_{sp^3} components as a function of annealing temperature. The changes in relative intensities are large until 650 K. Beyond that the relative intensities are almost constant. The strong initial decrease of the FWHM is caused by the decrease of the relative intensity of the C_{sp^3} component, while the decrease above 850 K is due to a decrease in the Gaussian FWHM of the C_{sp^2} component, indicating further reconfiguration in the carbon membrane toward a more uniform embedding matrix.

Lastly, the corresponding Ir $4f_{7/2}$ core level fits are plotted in Figures 8d and 8e. The quantitative analysis in Figure 8f shows the normalized intensities of the Ir_S and Ir_{int} components as a function of temperature. Up to 850 K the two components evolve complementary—Ir_S increases and Ir_{int} decreases. Our interpretation is as follows: Upon annealing, the entire membrane reorganizes, whereby the binding between the membrane and the Ir substrate is weakened. Considering that binding of h-BN normal to its plane, i.e., to the substrate and to cluster and a-C matrix, is through the sp^3 binding motif, a weakened binding of h-BN to Ir(111) implies thus also a weakened binding of h-BN to clusters and the a-C matrix. Indeed, the absence of all indications for C−N and C−B bonds in the C 1s spectra after annealing is consistent with this interpretation. Also, scratching experiments with the STM tip

show that the embedding matrix together with the clusters can be removed from the h-BN after heating (compare Figure S3), while this is impossible when Gr is used as a 2D layer.[14] Thus, it appears open whether a lift-off procedure will delaminate the membrane between Ir(111) and the 2D layer—as for Gr—or between the 2D layer and the a-C matrix with the enclosed clusters. The latter would be in fact not unwanted when considering the potential use of the membrane for electro-catalysis, where the Pt metal cluster must display an open surface exposed to the reactants. Experiments to explore the lift-off of the cluster superlattice membrane with h-BN as a 2D layer after annealing to ∼850 K are therefore of great interest. Heating beyond 850 K causes intercalation of the Pt cluster material, whereby Ir_{int} decreases—the component character-istic for clusters present in the valleys of the h-BN layer. Ir_S decreases as well, since the intercalated Pt now forms bonds with the surface atoms, whereby these Ir atoms do not contribute anymore to Ir_S.

■ CONCLUSIONS

We established, through STM topographs and XPS core level analysis, three regimes in the carbon embedding process of cluster superlattices templated on h-BN on Ir(111). First, the incoming carbon binds to the metal clusters and the sp^3 rehybridized area along their rim. This process also leads to a reshaping from the metastable monolayer clusters into multilayer clusters. Second, further C deposition onto the covered clusters then leads to an increase in valley size as more h-BN becomes sp^3-hybridized. The geometry for hybridization of the h-BN becomes less favorable further away from the original valley and thus limits the amount of C that can form bonds to the h-BN. Third, after all possible bonds are saturated, C starts forming a closed carbon film, which is tunable in thickness and consists mostly of sp^2- and sp^3-hybridized carbon compounds. The thermal stability and evolution of the cluster membrane were studied via the same methods, and the embedded clusters were found to be stable up to 850 K. After annealing to this temperature, the amorphous carbon matrix was shown to form a more coherent sp^2/sp^3-hybridized carbon membrane which is only loosely

bound to the h-BN. Above 850 K the clusters decay via intercalation between h-BN and the Ir substrate. Some clusters remain in the matrix until the highest observed temperature of 1250 K.

ASSOCIATED CONTENT

Supporting Information

The Supporting Information is available free of charge at https://pubs.acs.org/doi/10.1021/acs.jpcc.1c06829.

Reciprocal space map of the ($H = 0$, K, L) plane of a C-embedded cluster superlattice; XP spectra of the C 1s core level of carbon deposited directly on h-BN/Ir(111); STM topograph of a C-embedded cluster superlattice on h-BN/Ir(111) after scratching the surface with the STM tip (PDF)

AUTHOR INFORMATION

Corresponding Author

Tobias Hartl − *II. Physikalisches Institut, University of Cologne, 50937 Cologne, Germany;* orcid.org/0000-0002-3881-5462; Phone: +49 (0)221 470-3480; Email: hartl@ph2.uni-koeln.de

Authors

Moritz Will − *II. Physikalisches Institut, University of Cologne, 50937 Cologne, Germany;* orcid.org/0000-0003-4822-9122

Pantelis Bampoulis − *II. Physikalisches Institut, University of Cologne, 50937 Cologne, Germany; Physics of Interfaces and Nanomaterials, MESA+ Institute for Nanotechnology, University of Twente, 7500 AE Enschede, The Netherlands*

Daniel Herrmann − *II. Physikalisches Institut, University of Cologne, 50937 Cologne, Germany*

Philipp Valerius − *II. Physikalisches Institut, University of Cologne, 50937 Cologne, Germany*

Charlotte Herbig − *II. Physikalisches Institut, University of Cologne, 50937 Cologne, Germany; Department of Physics, University of California, Berkeley, Berkeley, California 94720, United States*

Virginia Boix de la Cruz − *Division of Synchrotron Radiation Research, Lund University, SE-22100 Lund, Sweden;* orcid.org/0000-0002-1152-8201

Paolo Lacovig − *Elettra-Sincrotrone Trieste S.C.p.A., I-34149 Trieste, Italy;* orcid.org/0000-0001-7001-7930

Vedran Vonk − *Deutsches Elektronen-Synchrotron (DESY), 22607 Hamburg, Germany;* orcid.org/0000-0001-9854-1101

Simon Chung − *Deutsches Elektronen-Synchrotron (DESY), 22607 Hamburg, Germany;* orcid.org/0000-0001-8087-8793

Andreas Stierle − *Deutsches Elektronen-Synchrotron (DESY), 22607 Hamburg, Germany;* orcid.org/0000-0002-0303-6282

Silvano Lizzit − *Elettra-Sincrotrone Trieste S.C.p.A., I-34149 Trieste, Italy*

Jan Knudsen − *Division of Synchrotron Radiation Research, Lund University, SE-22100 Lund, Sweden; MAX IV Laboratory, Lund University, SE-22100 Lund, Sweden*

Thomas Michely − *II. Physikalisches Institut, University of Cologne, 50937 Cologne, Germany*

Complete contact information is available at:
https://pubs.acs.org/10.1021/acs.jpcc.1c06829

Notes

The authors declare no competing financial interest.

DEDICATION

This paper is dedicated to the memory of our colleague and friend Patrica A. Thiel, who passed away in September 2020.

REFERENCES

(1) Yankowitz, M.; Chen, S.; Polshyn, H.; Zhang, Y.; Watanabe, K.; Taniguchi, T.; Graf, D.; Young, A. F.; Dean, C. R. Tuning superconductivity in twisted bilayer graphene. *Science* 2019, 363, 1059−1064.

(2) Yang, Y.; Hillmann, R.; Qi, Y.; Korzetz, R.; Biere, N.; Emmrich, D.; Westphal, M.; Büker, B.; Hütten, A.; Beyer, A.; et al. Ultrahigh Ionic Exclusion through Carbon Nanomembranes. *Adv. Mater.* 2020, 32, 1907850.

(3) Naberezhnyi, D.; Gölzhäuser, A.; Dementyev, P. Water-Assisted Permeation of Gases in Carbon Nanomembranes. *J. Phys. Chem. Lett.* 2019, 10, 5598−5601.

(4) Hartl, T.; Will, M.; Capeta, D.; Singh, R.; Scheinecker, D.; Boix de la Cruz, V.; Dellmann, S.; Lacovig, P.; Lizzit, S.; Senkovskiy, B. V.; et al. Cluster Superlattice Membranes. *ACS Nano* 2020, 14, 13629−13637.

(5) Ren, X.; Lv, Q.; Liu, L.; Liu, B.; Wang, Y.; Liu, A.; Wu, G. Current progress of Pt and Pt-based electrocatalysts used for fuel cells. *Sustain. Energy Fuels* 2020, 4, 15−30.

(6) Kodama, K.; Nagai, T.; Kuwaki, A.; Jinnouchi, R.; Morimoto, Y. Challenges in applying highly active Pt-based nanostructured catalysts for oxygen reduction reactions to fuel cell vehicles. *Nat. Nanotechnol.* 2021, 16, 140−147.

(7) Knudsen, J.; Feibelman, P. J.; Gerber, T.; Grånäs, E.; Schulte, K.; Stratmann, P.; Andersen, J. N.; Michely, T. Clusters binding to the graphene moiré on Ir (111): X-ray photoemission compared to density functional calculations. *Phys. Rev. B: Condens. Matter Mater. Phys.* 2012, 85, 035407.

(8) N'Diaye, A. T; Gerber, T.; Busse, C.; Myslivecek, J.; Coraux, J.; Michely, T. A versatile fabrication method for cluster superlattices. *New J. Phys.* 2009, 11, 103045.

(9) Donner, K.; Jakob, P. Structural properties and site specific interactions of Pt with the graphene/Ru (0001) moiré overlayer. *J. Chem. Phys.* 2009, 131, 164701.

(10) Sitja, G.; Bailly, A.; De Santis, M.; Heresanu, V.; Henry, C. R. Regular Arrays of Pt Clusters on Alumina: A New Superstructure on Al2O3/Ni3Al (111). *J. Phys. Chem. C* 2019, 123, 24487−24494.

(11) Düll, F.; Freiberger, E. M.; Bachmann, P.; Steinhauer, J.; Papp, C. Pt Nanoclusters Sandwiched between Hexagonal Boron Nitride and Nanographene as van Der Waals Heterostructures for Optoelectronics. *ACS Appl. Nano Mater.* 2019, 2, 7019−7024.

(12) Düll, F.; Steinhauer, J.; Späth, F.; Bauer, U.; Bachmann, P.; Steinrück, H.-P.; Wickert, S.; Denecke, R.; Papp, C. Ethylene: Its adsorption, reaction, and coking on Pt/h-BN/Rh (111) nanocluster arrays. *J. Chem. Phys.* 2020, 152, 224710.

(13) Will, M.; Hartl, T.; Boix de la Cruz, V.; Lacovig, P.; Lizzit, S.; Knudsen, J.; Michely, T.; Bampoulis, P. Growth, Stability, and Electronic Decoupling of Pt Clusters on h-BN/Ir (111). *J. Phys. Chem. C* 2021, 125, 3880.

(14) Will, M.; Bampoulis, P.; Hartl, T.; Valerius, P.; Michely, T. Conformal Embedding of Cluster Superlattices with Carbon. *ACS Appl. Mater. Interfaces* **2019**, *11*, 40524–40532.

(15) Farwick zum Hagen, F. H.; Zimmermann, D. M.; Silva, C. C.; Schlueter, C.; Atodiresei, N.; Jolie, W.; Martinez-Galera, A. J.; Dombrowski, D.; Schroder, U. A.; Will, M.; et al. Structure and growth of hexagonal boron nitride on Ir (111). *ACS Nano* **2016**, *10*, 11012–11026.

(16) Horcas, I.; Fernández, R.; Gomez-Rodriguez, J.; Colchero, J.; Gómez-Herrero, J.; Baro, A. WSXM: a software for scanning probe microscopy and a tool for nanotechnology. *Rev. Sci. Instrum.* **2007**, *78*, 013705.

(17) Franz, D.; Runte, S.; Busse, C.; Schumacher, S.; Gerber, T.; Michely, T.; Mantilla, M.; Kilic, V.; Zegenhagen, J.; Stierle, A. Atomic structure and crystalline order of graphene-supported Ir nanoparticle lattices. *Phys. Rev. Lett.* **2013**, *110*, 065503.

(18) Orlando, F.; Larciprete, R.; Lacovig, P.; Boscarato, I.; Baraldi, A.; Lizzit, S. Epitaxial growth of hexagonal boron nitride on Ir (111). *J. Phys. Chem. C* **2012**, *116*, 157–164.

(19) Will, M.; Atodiresei, N.; Caciuc, V.; Valerius, P.; Herbig, C.; Michely, T. A monolayer of hexagonal boron nitride on Ir (111) as a template for cluster superlattices. *ACS Nano* **2018**, *12*, 6871–6880.

(20) Hu, A.; Rybachuk, M.; Alkhesho, I.; Lu, Q.-B.; Duley, W. Nanostructure and sp 1/sp 2 clustering in tetrahedral amorphous carbon thin films grown by femtosecond laser deposition. *J. Laser Appl.* **2008**, *20*, 37–42.

(21) Rodriguez, N.; Anderson, P.; Wootsch, A.; Wild, U.; Schlögl, R.; Paál, Z. XPS, EM, and catalytic studies of the accumulation of carbon on Pt black. *J. Catal.* **2001**, *197*, 365–377.

(22) Weltner, W., Jr.; Van Zee, R. J. Carbon molecules, ions, and clusters. *Chem. Rev.* **1989**, *89*, 1713–1747.

(23) Chavanne, A.; Arnault, J.-C.; Barjon, J.; Arabski, J. Bias-enhanced nucleation of diamond on iridium: A comprehensive study of the first stages by sequential surface analysis. *Surf. Sci.* **2011**, *605*, 564–569.

(24) Herbig, C.; Knispel, T.; Simon, S.; Schroeder, U. A.; Martinez-Galera, A. J.; Arman, M. A.; Teichert, C.; Knudsen, J.; Krasheninnikov, A. V.; Michely, T. From permeation to cluster arrays: graphene on Ir (111) exposed to carbon vapor. *Nano Lett.* **2017**, *17*, 3105–3112.

(25) Björneholm, O.; Nilsson, A.; Tillborg, H.; Bennich, P.; Sandell, A.; Hernnäs, B.; Puglia, C.; Mårtensson, N. Overlayer structure from adsorbate and substrate core level binding energy shifts: CO, CCH3 and O on Pt (111). *Surf. Sci.* **1994**, *315*, L983–L989.

(26) Yan, X.; Xu, T.; Chen, G.; Yang, S.; Liu, H.; Xue, Q. Preparation and characterization of electrochemically deposited carbon nitride films on silicon substrate. *J. Phys. D: Appl. Phys.* **2004**, *37*, 907.

(27) Ottaviani, B.; Derré, A.; Grivei, E.; Mahmoud, O. A. M.; Guimon, M.-f.; Flandrois, S.; Delhaès, P. Boronated carbons: structural characterization and low temperature physical properties of disordered solids. *J. Mater. Chem.* **1998**, *8*, 197–203.

(28) Oliveira, M. N.; Botelho do Rego, A. M.; Conde, O. XPS investigation of BxNyCz coatings deposited by laser assisted chemical vapour desposition. *Surf. Coat. Technol.* **1998**, *100-101*, 398–403.

(29) Sutter, P.; Sutter, E. Thickness determination of few-layer hexagonal boron nitride films by scanning electron microscopy and Auger electron spectroscopy. *APL Mater.* **2014**, *2*, 092502.

(30) Lii-Rosales, A.; Han, Y.; Evans, J. W.; Jing, D.; Zhou, Y.; Tringides, M. C.; Kim, M.; Wang, C.-Z.; Thiel, P. A. Formation of multilayer Cu islands embedded beneath the surface of graphite: characterization and fundamental insights. *J. Phys. Chem. C* **2018**, *122*, 4454–4469.

(31) Liu, Y.; Liu, X.; Wang, C.-Z.; Han, Y.; Evans, J. W.; Lii-Rosales, A.; Tringides, M. C.; Thiel, P. A. Mechanism of Metal Intercalation under Graphene through Small Vacancy Defects. *J. Phys. Chem. C* **2021**, *125*, 6954–6962.

(32) Sicot, M.; Leicht, P.; Zusan, A.; Bouvron, S.; Zander, O.; Weser, M.; Dedkov, Y. S.; Horn, K.; Fonin, M. Size-selected epitaxial nanoislands underneath graphene moiré on Rh (111). *ACS Nano* **2012**, *6*, 151–158.

(33) Coraux, J.; N'Diaye, A. T.; Rougemaille, N.; Vo-Van, C.; Kimouche, A.; Yang, H.-X.; Chshiev, M.; Bendiab, N.; Fruchart, O.; Schmid, A. K. Air-protected epitaxial graphene/ferromagnet hybrids prepared by chemical vapor deposition and intercalation. *J. Phys. Chem. Lett.* **2012**, *3*, 2059–2063.

(34) Schumacher, S.; Huttmann, F.; Petrović, M.; Witt, C.; Förster, D. F.; Vo-Van, C.; Coraux, J.; Martinez-Galera, A. J.; Sessi, V.; Vergara, I.; et al. Europium underneath graphene on Ir (111): Intercalation mechanism, magnetism, and band structure. *Phys. Rev. B: Condens. Matter Mater. Phys.* **2014**, *90*, 235437.

(35) Boukhvalov, D.; Katsnelson, M. Destruction of graphene by metal adatoms. *Appl. Phys. Lett.* **2009**, *95*, 023109.